# scientific reports



# **OPEN**

# Resting-state functional MRI of the nose as a novel investigational window into the nervous system

Sara Ponticorvo<sup>1</sup>, Jaakko Paasonen<sup>2</sup>, Petteri Stenroos<sup>2</sup>, Raimo A. Salo<sup>2</sup>, Heikki Tanila<sup>2</sup>, Pavel Filip<sup>1,3</sup>, Douglas L. Rothman<sup>4</sup>, Lynn E. Eberly<sup>1,5</sup>, Michael Garwood<sup>1</sup>, Gregory J. Metzger<sup>1</sup>, Olli Gröhn<sup>2</sup>, Shalom Michaeli<sup>1,6</sup> & Silvia Mangia<sup>1,6</sup> ≅

Besides being responsible for olfaction and air intake, the nose contains abundant vasculature and autonomic nervous system innervations, and it is a cerebrospinal fluid clearance site. Therefore, the nose is an attractive target for functional MRI (fMRI). Yet, nose fMRI has not been possible so far due to signal losses originating from nasal air-tissue interfaces. Here, we demonstrated feasibility of nose fMRI by using novel ultrashort/zero echo time (TE) MRI. Results obtained in the resting-state from 13 healthy participants at 7T and in 5 awake mice at 9.4T revealed a highly reproducible resting-state nose functional network that likely reflects autonomic nervous system activity. Another network observed in humans involves the nose, major brain vessels and CSF spaces, presenting a temporal dynamic that correlates with heart rate and breathing rate. These resting-state nose functional signals should help elucidate peripheral and central nervous system integrations.

The nose is the major organ responsible for olfaction and air intake, which primarily engage two of four distinct types of epithelia found in the nasal cavity, namely the olfactory and respiratory epithelium, respectively. Interestingly, the nasal cavity contains a complex neuronal system extending to both olfactory and respiratory epithelium. The former, in particular, is innervated by branches of the trigeminal nerve<sup>1</sup>, the largest of the cranial nerves, carrying motor fibers to the muscles of mastication and transmitting sensory information from the face, scalp, mouth, and nasal passages to the central nervous system (CNS)<sup>2</sup>. Also, the nasal cavity contains neural innervation from parasympathetic and sympathetic systems, comprising the autonomic nervous system (ANS), that maintain turbinate functions<sup>3</sup> such as nasal secretions, patency, warmth, and humidification<sup>4</sup>. Those traits highlight the growing recognition of the nose as a crucial focal point for investigating the interplay between the peripheral and central nervous systems, as well as for elucidating disease mechanisms. Furthermore, concurrent impairment in both olfaction and autonomic functions frequently occurs during the early stages or during the progression of neurodegenerative disorders, as in the case of Parkinson's disease<sup>5-7</sup> and Alzheimer's disease<sup>8,9</sup>, further supporting the notion of a direct link between the nasal activity and the nervous system. Besides, according to the olfactory vector hypothesis, the nose can be seen as an important entry point for neurotropic agents that may cause or catalyze those neurodegenerative disorders 10. Yet, the characterization of system-wide functional connections between the nose and the nervous system is challenged by the lack of imaging methods that detect robust surrogates of neural activity in the nose.

One of the most powerful and flexible tools to study CNS activity is functional MRI (fMRI), which nonetheless has remained intrinsically inadequate for detecting nose functional signals. In fact, fMRI techniques that rely on the use of an echo time, such as gradient echo (GE)- or spin echo (SE)- echo planar imaging (EPI) widely used to measure blood-oxygenation-level-dependent (BOLD) signals<sup>11</sup>, suffer from image distortions and signal losses caused by magnetic field inhomogeneities<sup>12</sup>. Offline strategies have been developed for correcting image distortions, for example by characterizing field inhomogeneities using a field map<sup>13</sup>, or by generating a map of displacement field by collecting two images with opposite phase encoding directions<sup>14</sup>. Both approaches estimate a distortion map that can be used to correct (unwarp) the original images. However, they are ineffective in frontal brain areas and especially the nose where the susceptibility artifacts originating from the air-tissue interfaces of the nasal cavity destroy magnetic field uniformity and, ultimately, the signal itself. To overcome

<sup>1</sup>Department of Radiology, Center for Magnetic Resonance Research, University of Minnesota, Minneapolis, MN, USA. <sup>2</sup>A. I. Virtanen Institute for Molecular Sciences, University of Eastern Finland, Kuopio, Finland. <sup>3</sup>Neurology, General University Hospital, Charles University, Prague, Czech Republic. <sup>4</sup>Department of Radiology and Biomedical Imaging, Magnetic Resonance Research Center, Yale University, New Haven, CT, US. <sup>5</sup>Division of Biostatistics, School of Public Health, University of Minnesota, Minneapolis, MN, USA. <sup>6</sup>These authors contributed equally:Shalom Michaeli and Silvia Manqia. <sup>∞</sup>email: manqia@umn.edu

the challenges caused by susceptibility inhomogeneities, one can use acquisitions schemes that do not rely on the formation of an echo, such as in ultrashort echo time (UTE)<sup>15-17</sup>, zero echo time (ZTE)<sup>18</sup> or SWeep Imaging with Fourier Transform (SWIFT)<sup>19,20</sup> techniques. Importantly, previous studies in anesthetized rats<sup>21</sup> and head-fixed awake rats<sup>22</sup> at 9.4T have convincingly demonstrated that fMRI contrast is not only feasible, but highly advantageous with a zero-TE technique such as Multi-Band SWIFT (MB-SWIFT) and that it is mostly related to blood flow and volume. The benefits of MB-SWIFT are indeed numerous, including its compatibility with electrophysiological recordings, its resilience to susceptibility artefacts including those induced by metallic implants and body movements, and, finally, its inherent quietness that improves subject comfort, compliance and minimizes unintended activations due to gradient induced noise. However, applications of ultrashort/zero-TE techniques to fMRI in humans remain limited<sup>23,24</sup>, and applications to study nasal functional signals have not yet been explored.

In this study, we aim to demonstrate the feasibility of ultrashort/zero-TE techniques to detect nasal functional signals and their brain connections in human and animal models in resting awake conditions. With the goal of characterizing the physiological correlates of the nasal signals, corresponding cardiac and respiratory data were acquired. We propose that the nasal resting-state functional networks will help elucidate unique interactions between the peripheral and central nervous systems in health and disease.

#### Results

# UTE unveils two functional networks involving the nose in humans

Raw images

The field of view used in the UTE acquisitions included both the brain and nose for all participants. All data were of sufficient quality (e.g., without motion artifacts), and were thus included in further analyses. Raw images from one representative subject are displayed in Fig. 1, from which it can be seen that with standard GE-EPI (TE=22.2 ms) no signal is detected in the nose (Fig. 1A and D), whereas a clear signal and anatomical details are visible when the images are acquired with UTE, both in the low-resolution fMRI setup (TE=0.12 ms, Fig. 1B and E) and in the high-resolution anatomical setup (TE=0.11 ms, Fig. 1C and F). Therefore, by using MRI sequences that do not rely on an echo, we demonstrate that it is possible to detect functional and anatomical

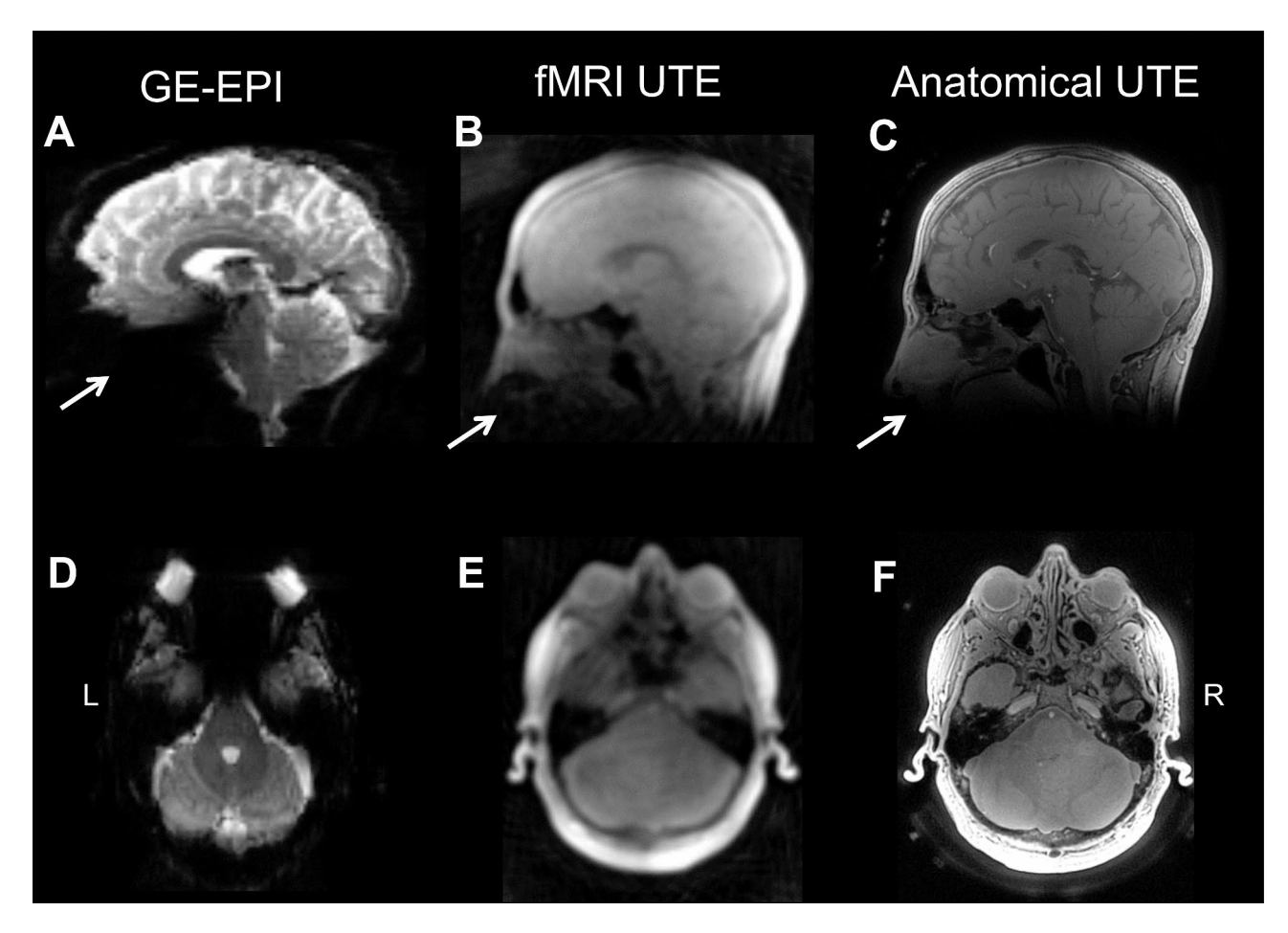


**Fig. 1.** Comparison of raw images GE-EPI vs. UTE. Brain images are acquired from the same slice in one representative subject at 7T with GE-EPI (**A** and **D**), UTE with fMRI resolution (**B** and **E**) and UTE with anatomy resolution (**C** and **F**). Sagittal views (**A**–**C**) and axial views (**D**–**F**). Whereas GE-EPI shows large areas of signal dropout in the nose (white arrow), these are almost completely eliminated with UTE.

signals from the nasal area with reduced distortion compared to GE-EPI that on the other hand suffers for increased sensitivity to susceptibility differences resulting from the abundant tissue-air interfaces.

#### Group level resting-state fMRI with UTE and GE-EPI

Group-level independent component analysis (ICA) of resting-state fMRI data from the 13 human participants demonstrate that it is possible to identify a prominent network in the nasal cavity with UTE (Fig. 2A) that is not visible with GE-EPI (Fig. 2E). Compared with GE-EPI, UTE better shows a network extending to the cerebrospinal fluid (CSF) and the perivascular space around the brainstem with opposite polarity compared to the major vessels of the brain (Fig. 2B and F). Conventional resting-state functional components are also visible with UTE, including the CSF component (Fig. 2C), and, when the analysis is limited to the brain only, the default mode network (DMN, Fig. 2D), similarly to standard GE-EPI acquisitions (Fig. 2G and H, respectively). Notably, the spatial registration methods routinely used for brain images do not work properly for the nose, leading to blurring in the nasal area of both functional and anatomical images shown in Fig. 2. This feature, in addition to physiological inter-subject variability of the nasal area, resulted in the nose component of vague shape (Fig. 1A), prompting us to proceed with voxel-wise analyses at single-subject level.

#### Single-subject resting-state fMRI with UTE

Single-subject ICA results obtained from the resting-state fMRI UTE data of each participant were visually inspected by at least two independent researchers to ensure good data quality, and to manually select robust ICs of interest involving the nose. Such nose networks were very similar with either 20 or 30 ICs used in the ICA (data not shown); results that follow use networks identified from 30 ICs.

Among the obtained components, we consistently identified two networks involving the nose (Supplementary material from Supplementary Figure S1 to Supplementary Figure S37) similar to those detected in the group analysis (Fig. 2). The first network (Fig. 3A), called here "nose network", encompasses the entire nasal cavity and it is apparently unilateral (in 11 out of 13 subjects), possibly reflecting the side of the nose that is actively receiving respiration according to the nasal cycle. The second network (Fig. 3B), called here "CSF/Vessels network", encompasses the CSF in the perivascular space around the brainstem, and, with opposite polarity, the major brain vessels and partially the nose - albeit with varying extension and location across subjects. While the time evolution of the nose network is characterized by very slow fluctuations that resemble those of the heart rate and breathing rate variability (HRV and BRV, respectively), the CSF/Vessels network is characterized by high- and low-frequency fluctuations similar to heart rate and breathing rates (Fig. 3C).

When overlaying the IC maps on the anatomical UTE images, which provide more anatomical contrast and details in the nose area, it is obvious that the nose network is not only lateralized but is positioned on the nasal cavity side that was more open during the scan, as it is visible in the high anatomical resolution UTE image (Fig. 4 for one representative subject data and figures S1 to S37 for all the subjects).

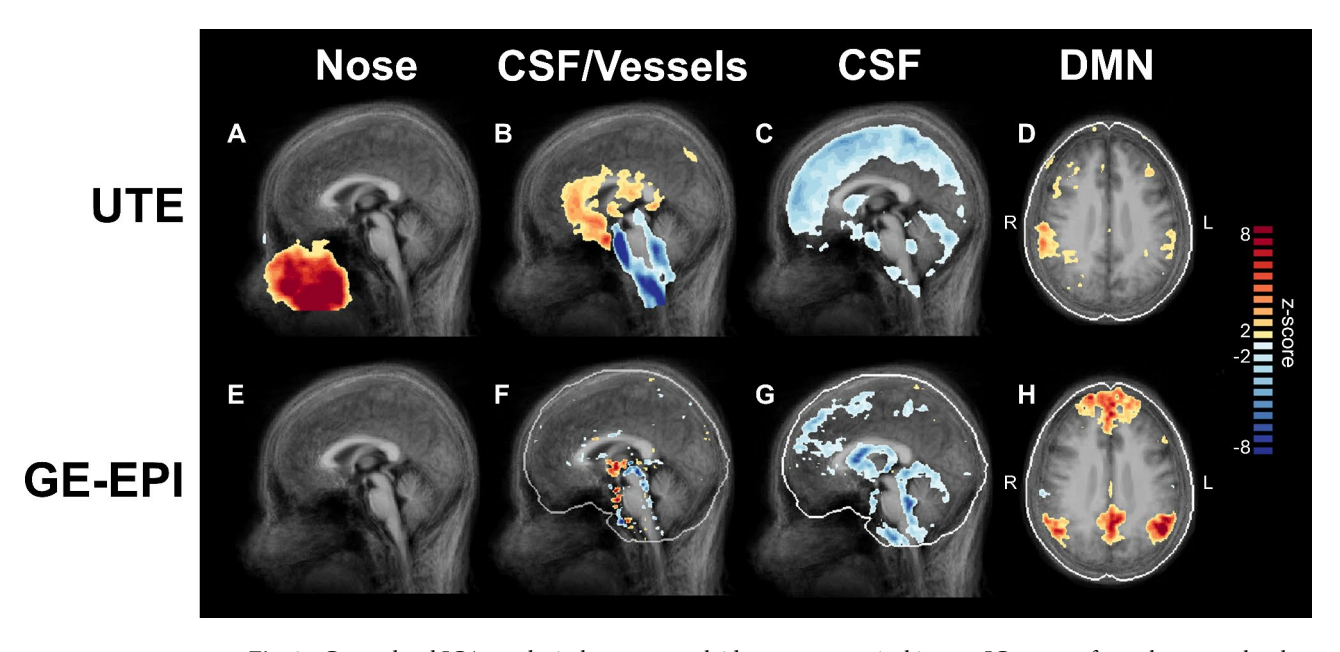


**Fig. 2.** Group-level ICA results in humans overlaid on an anatomical image. IC z-maps from the group-level analysis (n = 13) on both UTE (**A-D**) and GE-EPI (**E-H**) data. Only the first run out of 3 runs were used for the group-level UTE group analysis. Components of interest include the nose network (**A** and **E**) only visible with UTE acquisition, the CSF/Vessels network (**B** and **F**), the CSF component (**C** and **G**) and the DMN (**D** and **H**). IC z-maps are overlaid on the average (across subjects) anatomical MP2RAGE.

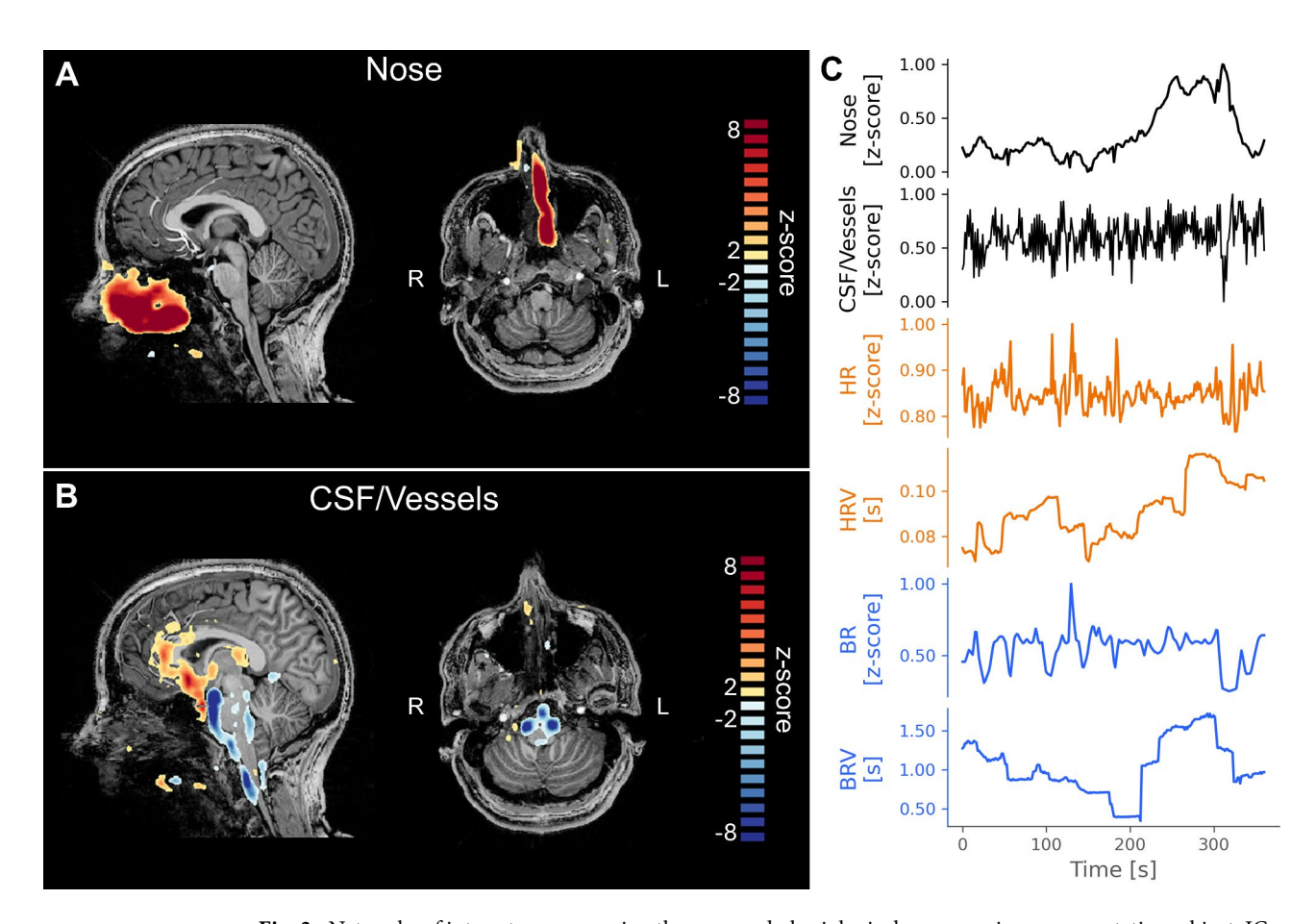


**Fig. 3**. Networks of interest encompassing the nose and physiological measures in a representative subject. ICs of interest from one representative human participant. IC z-maps representing the nose network (**A**) and the CSF/Vessels network (**B**) are overlaid on the anatomical MP2RAGE images, both presented in sagittal and axial view. Panel (**C**) shows all the time-courses of interest: IC time-courses (black), pulse measures (orange) of heart rate (HR) and heart rate variability (HRV), respiration measures (blue) of breathing rate (BR) and breathing rate variability (BRV). The unilateral nose component appears to be located on the side with the more open nostril, as it can be seen in axial view.

# Correlations with physiological signals

Physiological data (respiration and peripheral pulse signals) were available in full for 29 UTE scans (3 runs from 9 subjects and 2 runs from 1 subject) and in a shorter version, due to technical problems, during 5 scans (1 run from 2 subjects and 3 runs for one subject).

When available, Pearson's correlation coefficients were calculated between each resting-state fMRI time-courses and each physiological measure, separately for each subject and run. The results of the correlation analysis are shown in Supplementary Figure S38. From the linear mixed model analysis at the group level, the nose network time-course was significantly correlated with HRV (t-value=-4.39,  $p=1.15e^{-5}$ ) and BRV (t-value=11.1,  $p=2.52e^{-28}$ ) but not with HR (t-value=-1.26, p=0.21) or BR (t-value=1.30, p=0.19), while the CSF/Vessels network time-course was significantly correlated with HR (t-value=-5.63,  $p=1.85e^{-8}$ ) and BR (t-value=-2.5, p=0.012) but not with HRV (t-value=2.0, p=0.04) or BRV (t-value=-1.48, p=0.14). Therefore, the temporal signal of the nose network appears to be synchronized with the variability in breathing and heart rates but not the rates themselves, while the opposite is true for the CSF/Vessels network.

# Intra-subject reproducibility of the nose network and the CSF/Vessels network

All subjects except one completed 3 UTE runs, used to assess intra-subject reproducibility. The two ICs of interest involving the nose were found in each subject and run. Single-subject maps of the nose and CSF/Vessels networks are shown in Fig. 5A and C, respectively, for one representative subject. Eight subjects (out of 12) showed consistent unilateral nose networks in all the 3 runs; one subject showed consistent bilateral nose network in all the 3 runs; finally, one subject showed the nose network (bilateral) only in 1 run, while one subject showed a change from bilateral to unilateral network across runs (Figures S1 to S37). To quantify the intrasubject reproducibility, the dice similarity coefficient was calculated for each pair of runs (run 1 vs. run 2; run 1 vs. run 3; run 2 vs. run 3) for each subject. The average dice coefficient (mean  $\pm$  sd, range) across subjects and run pairs is  $0.47 \pm 0.21$ , 0.058 - 0.871 for the nose network (Fig. 5B) and  $0.63 \pm 0.11$ , 0.374 - 0.829 for the CSF/Vessels network (Fig. 5D), indicating good reproducibility across scans for both networks.

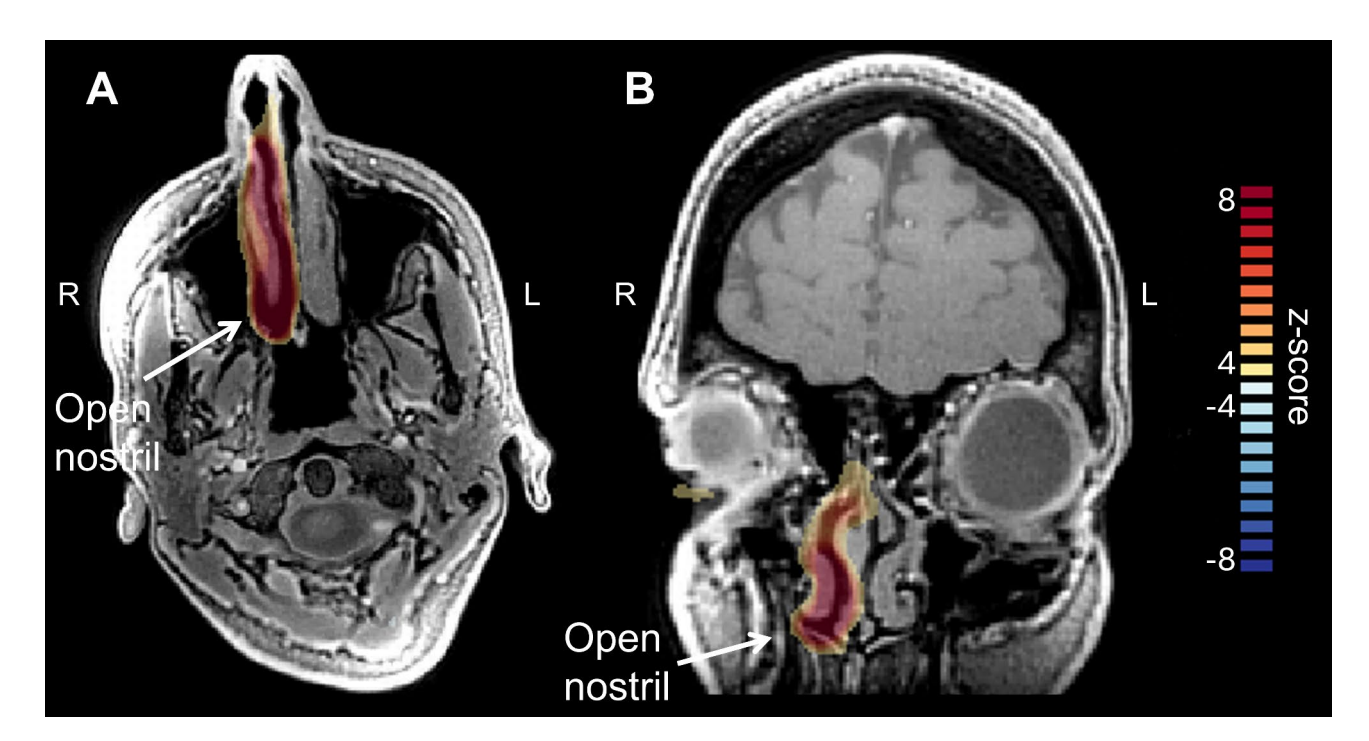


**Fig. 4.** Anatomical details of the nose network in humans. Nose IC details of one representative subject are overlaid on high-resolution UTE images in axial (**A**) and sagittal (**B**) views, which reinforce the signal's correspondence to anatomical details. The unilateral nose component appears to be located on the side of the open nostril as can be seen in axial view.

Effect of removal of physiological signals from the resting-state signals

Physiological confounds were removed from rsfMRI data using different strategies. When complete physiological signals were recorded (29 scans), those signals were used to assess their effects on the resting-state fMRI UTE data. From the fMRI data, we linearly regressed out either the physiological signals modeled with RETROICOR (method for retrospective correction of physiological motion effects in fMRI)<sup>25</sup>, or the HRV and BRV signals. An additional analysis was performed with a data-driven approach by regressing out confound signals calculated as mean time-courses in white matter and CSF voxels. In order to quantify the reproducibility of the networks across preprocessing pipelines, for each scan and network, we calculated the dice similarity coefficient between the original network (without any correction) and the network identified by ICA either after RETROICOR, after regressing out HRV and BRV, and after regressing out white matter and CSF signals. The original nose network (Fig. 6A) is virtually identical to those identified after RETROICOR (Fig. 6B), after regressing out HRV and BRV (Fig. 6C) and after regressing out white matter and CSF signals (Fig. 6D). The average dice similarity coefficient  $(\text{mean} \pm \text{sd}, \text{range})$  was also very high in all cases, namely  $0.89 \pm 0.11, 0.500 - 0.980$  (Fig. 6E),  $0.85 \pm 0.12, 0.454 -$ 0.986 (Fig. 6F), and  $0.89 \pm 0.14$ , 0.37 - 0.99 (Fig. 6G) respectively. Similar observations apply to the CSF/vessels network. The original map (Fig. 6H) is very similar to the map obtained after HRV and BRV are regressed out (Fig. 6J) and to the map obtained after white matter and CSF signals are regressed out (Fig. 6K), with a dice similarity index of  $0.91 \pm 0.09$ , 0.497 - 0.984 (Fig. 6M) and  $0.93 \pm 0.06$ , 0.64 - 0.98 (Fig. 6N), and to a lesser extent to the map obtained after RETROICOR (Fig. 6I). In the latter case, the network is not even recognized or severely altered in 3 scans, overall leading to a lower dice coefficient of 0.58 ± 0.29, 0.090-0.960 (Fig. 6L). The effects of physiological corrections on the first run of each subject are shown in Supplementary Figure S39 (nose component) and Supplementary Figure S40 (CSF/Vessels component).

## MB-SWIFT unveils nose functional parcellation in awake mice

The resting-state fMRI data in awake head-fixed mice were acquired with the zero-TE technique MB-SWIFT. The data were analyzed with ICA using 30 ICs at both single-subject level and group level after spatial normalization. ICs were visually inspected independently by at least two researchers to ensure good data quality, and to manually select components of interest. At the group-level we detected multiple nose components (8 out of 30), which appear to provide a functional nose parcellation (Fig. 7A and Supplementary Figure S41). Similarly to the human data, mice data confirm that with zero-TE fMRI it is possible to detect standard brain networks as shown in Supplementary Figure S42. From the single subject analysis, similar (but mostly bilateral) resting-state networks, encompassing the nose area, were obtained in the awake mice as shown in Fig. 7B for one representative mouse and in Supplementary Figure S43 for all animals. On the selected single subject components, the average dice similarity coefficient calculated between each pair of subjects was (mean  $\pm$  sd, range) 0.49  $\pm$  0.05, 0.40–0.57 (Fig. 7c), indicating that similar nose component is consistently observed across different mice.

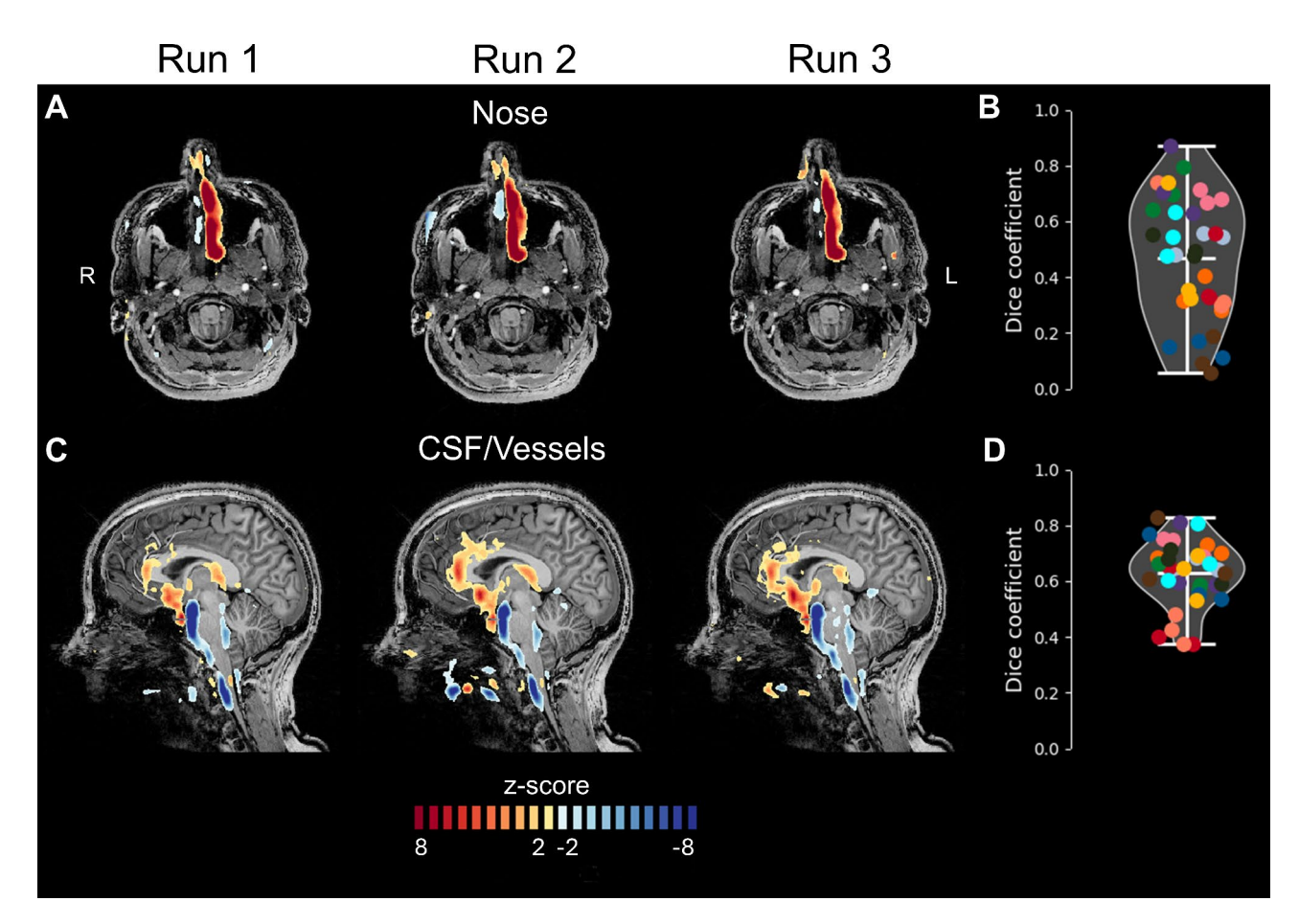


Fig. 5. Intra-subject reproducibility of networks encompassing the nose in humans. Nose (A, B) and CSF/ Vessels (C, D) networks reproducibility in the same representative subject. Twelve subjects (out of 13) underwent 3 UTE runs in the same session. Reproducibility was quantified with the dice similarity coefficient between each pair of runs for each subject for the nose component (B) and for the CSF/Vessels component (D). Each subject is represented by a different color and the violin plots show the values distribution (all subjects, all run pairs).

#### Discussion

In the current study, we demonstrate the feasibility of detecting reliable and reproducible functional signals in the nose of humans and mice when using MRI sequences with ultrashort/zero-TE. These results enable new explorations of relationships between nasal activity, brain activity<sup>26</sup>, and cognitive function<sup>27,28</sup> as well as potential applications to pathological conditions with known abnormal nasal function. Due to the connections of the nose to the ANS, exploiting the fMRI signal fluctuations in the nose can contribute to our overall understanding of the complex interactions between the peripheral and central nervous systems.

Functional MRI of the nose opens a new area of research, which hitherto has been precluded due to lack of appropriate imaging technology. Despite the fact that zero-TE fMRI has been used in other applications in rodents<sup>21,29–34</sup>, the implementation of this strategy to solve the challenges of MRI signal loss in the nose had not been presented so far. Moreover, only one fMRI study so far has been reported using 3D UTE in humans at 3T<sup>23</sup>. Interestingly, the authors detected only negative responses with visual stimulation, as opposite to the positive responses seen previously with SWIFT fMRI at 4T<sup>24</sup> during the same sensory stimulation. Most importantly, their study did not focus on detecting functional networks during the resting-state, neither did it focused on the nose areas, thus complicating the comparison with the results of the current study. On the other hand, the UTE implementation presented in this study enabled detection not only of nose signals, but also of standard brain networks (e.g. DMN and CSF component)<sup>35</sup> at group level, thus providing evidence to the fact that UTE can be sensitized to functional contrast in human applications. The sensitivity of UTE to hemodynamic signals linked to brain activity was most likely enhanced by the use of a slab selective RF pulse, which is expected to augment the role of blood inflow, even if we cannot rule out that other mechanisms may play a role as well, e.g., T1 relaxation processes or oxygenation, among others.

The data-driven analysis of the images produced by the UTE sequence in humans revealed the existence of a prominent, unilateral functional network that extended to one side of the nasal cavity and exhibited ultra-slow fluctuations. The signal time-course of this nose network correlated with BRV and HRV, the latter believed to reflect parasympathetic activity<sup>36</sup>, or generally ANS functions, which include regulating involuntary physiologic

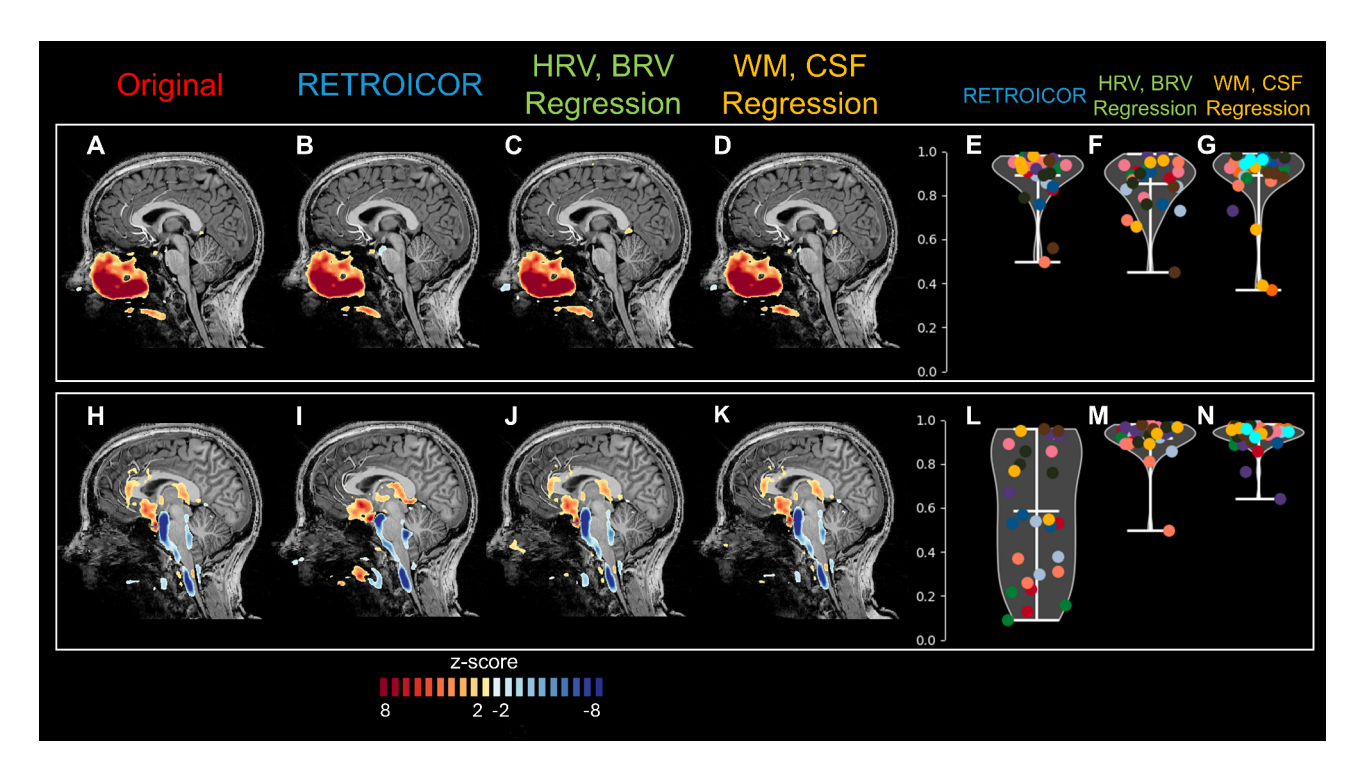
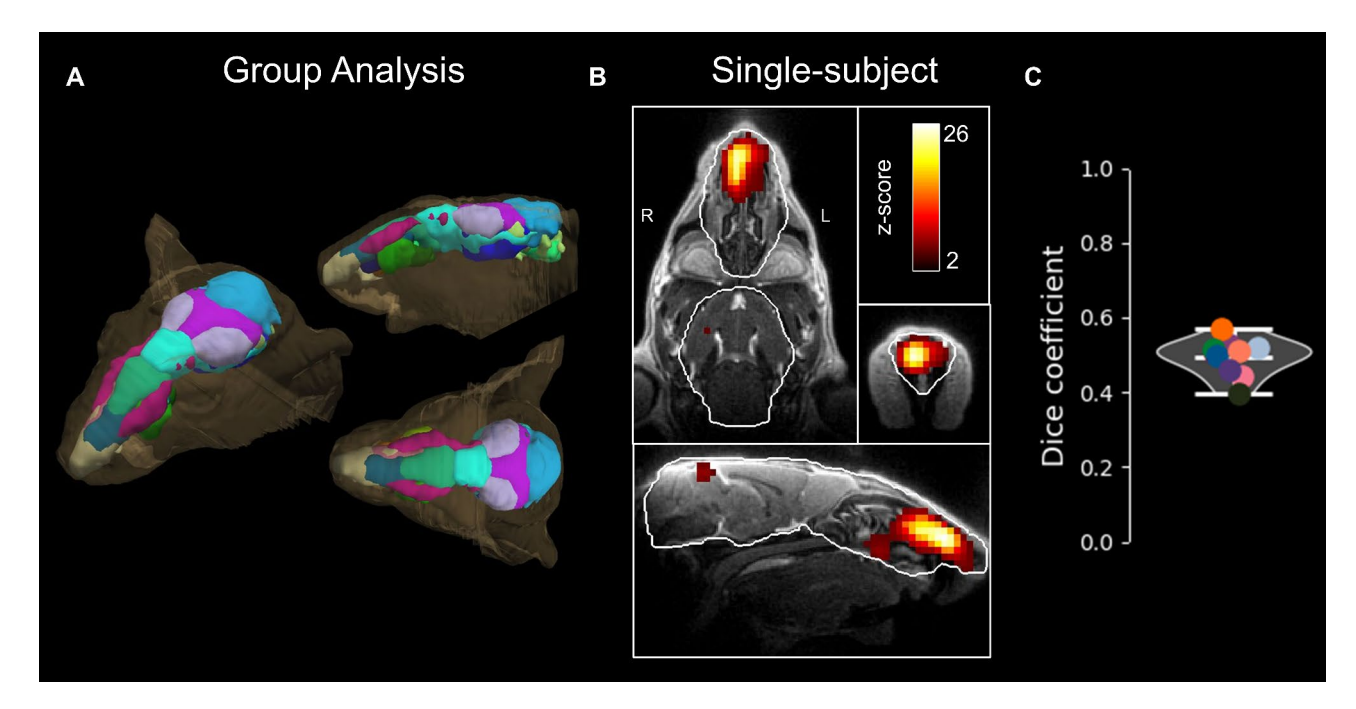


Fig. 6. Effect of removal of physiological signals. Reproducibility of ICs of interest, namely the nose network (A–G) and the CSF/Vessels network (H–N), when different noise corrections are performed. Z-maps are shown for one representative subject, while reproducibility of ICs was assessed at group-level with the dice similarity coefficient between the uncorrected components and the components estimated after each correction modality. The original nose component (A) is almost identical to the component obtained when RETROICOR correction is applied (B), when HRV and BRV are regressed out (C), when white matter and CSF signals are regressed out (D) and at group-level the dice coefficient is uniformly high (E–G). The original CSF/Vessels component (H) is almost identical to the component obtained when HRV and BRV are regressed out (J) when white matter and CSF signals are regressed out (K) and very similar when RETROICOR correction is applied (I). However, some variability across subjects/runs can be observed when RETROCOR is applied (L), which is not evident when HRV and BRV or white matter and CSF signals are regressed out (M and N). A total of 29 scans (3 runs from 9 subjects and 2 runs from 1 subject) had full physiological recording and therefore were used for the regression analysis with physiological signals.

processes, i.e., heart rate, blood pressure, and respiration<sup>37</sup>. When inspecting the spatial localization of the mostly unilateral nose network, we noticed that it overlaid to the side of the nose with an open nostril at the time of the MRI acquisition. This observation is consistent with the nasal cycle, namely the asymmetrical, spontaneous change between the left and right nostrils in nasal airflow that takes place over several hours<sup>38</sup> in humans, caused by alternate congestion and decongestion of the venous sinuses. The nasal cycle is controlled by the sympathetic ANS nerves that supply the nasal blood vessels<sup>39</sup>, and it is believed to originate from the vasomotor control areas of the medulla<sup>40</sup>. Thus, the lateralization of the nose fMRI network, which is observed in most of the human data, on the side of the open airway could reflect the functional activity of the ANS, which controls, among others, the turbinate activities. The lack of correlation between the nose signal and HR or BR reduces the likelihood that the signal is mainly or exclusively related to airflow during respiration. On the other hand, because HRV is a proxy of neurocardiac functions and it is related to heart-brain interactions and dynamic ANS processes<sup>36</sup>, the correlation observed between the nose network signal and HRV is consistent with the nose network activity reflecting the nervous system processes that control the heart pulsations and/or the respiration frequency.

Using a similar zero-TE MRI sequence, a prominent resting-state network located in the nasal cavity was found also in the fMRI images of awake mice. The cross-species similarity of this detected nose functional network substantially reinforces the findings in humans, and it opens the opportunity of using animal models in preclinical applications to elucidate the underpinnings of the nose network. Moreover, unlike humans who have highly variable noses in shape and size, mice of the same strain and in the same age range have very similar noses. This feature makes the spatial normalization across mice noses easier than in humans, and it ultimately allows for group-level voxel-wise analyses and more precise mapping of networks in nasal cavities that are currently impossible with human data. While the locations and reproducibility of the nose network were similar in mice and humans, the unilaterality of the network was different across species. In fact, whereas in humans the network is mostly unilateral (11 out of 13 subjects), in mice it is mostly bilateral, an observation that is likely due to differences in the nasal cycle across humans and mice. In fact, no direct evidence exists on the nasal cycle in mice, but preliminary studies in rats indicated nostril alternation every 30–85 min<sup>41</sup>, while a more recent study even reports the absence of the nasal cycle with a symmetric nasal air flow over an entire day



**Fig.** 7. Group-level and single-subject ICA results in awake mice. ICA results are shown for the group-level analysis (n = 8 datasets) (**A**) and for the single-subject analysis from one representative subject (**B**). ICA was performed using a manually drown mask covering brain and nose (white outline). Inter-subject reproducibility was quantified with dice similarity coefficient (**C**) between each pair of subjects. At group-level, multiple nose components were detected in the mouse nose which seems to provide a functional nose parcellation.

in awake rats<sup>42</sup>. On these premises, we can only hypothesize in mice either the absence of a nasal cycle, or the presence of a very short nasal cycle, which may change even multiple times during the MRI scan, thus leading to nose networks that appear to be bilateral.

The other network of interest identified in humans is the CSF/Vessels network, which extends from the cervical subarachnoid space to the main brain artery with opposite polarity, and partially to the nose. This component is highly reproducible across subjects and temporally correlates with both BR and HR. Interestingly, the opposite polarity between the CSF portion of the component and the arterial portion seems to support previous evidence that, to maintain a constant intracranial volume, cerebral vasodilation is accompanied by a significant reduction in the CSF partial volume, which results in an anticorrelation between the blood signal (cerebral blood flow) and the CSF signal (CSF flow)<sup>43</sup>. Although this anticorrelation has been observed by using indirect BOLD signals only during visual stimulation<sup>44</sup> or sleep<sup>45</sup>, namely when more pronounced changes in blood flow are induced by the tasks, we speculate that we are able to detect the same phenomenon, even at resting-state, thanks to the enhanced direct sensitivity of zero/ultrashort-TE to flow. Moreover, the CSF flow itself has been shown to be cardiac- as well as respiratory-driven<sup>46</sup>, an observation that may explain the temporal correlation between the CSF/Vessels time-course and HR and BR. Strong evidence in multiple species showed the existence of an olfactory drainage route of CSF through the cribriform plate into the lymphatic system of the nasal mucosa and epithelia<sup>47</sup>. In humans, dynamic 18 F-THK5117 PET even showed CSF signal intensity in the superior nasal turbinate<sup>48</sup>. It is thus possible that the nose functional signals may, at least partially, reflect the CSF flow and its transit through the nasal epithelium. Therefore, mapping a functional network related to CSF flow, blood flow, and their relationship opens new possibilities for exploring functional coupling and closely investigating CSF flow. This opportunity may be crucial for understanding various neurological diseases, including amyotrophic lateral sclerosis<sup>49</sup> and possibly Alzheimer's disease<sup>50–52</sup>.

The cardiac and respiration signals were taken into account in multiple ways. First, we derived the cardiac and breathing rates along with the temporal variability, and correlated such metrics with the fMRI signals to explore possible dependencies. Then, we calculated the low-order Fourier-series of cardiac and respiratory phases to enable the RETROICOR pipeline commonly used to denoise the MRI signal from physiological confounds. More in details, because high correlations were found between the nose functional signals and physiological measures, we conducted an exploratory investigation removing those physiological variability contributions from the fMRI signal, and we reanalyzed the data in three different scenarios: by linearly regressing out RETROICOR cardiac and respiratory predictors, by linearly regressing out HRV and BRV time-courses and by linearly regressing out white matter and CSF average time-courses. The nose network was reproducible across the preprocessing pipelines, underlying the stability of the network and most importantly that, although there is strong correlation between the network time-course and HRV and BRV, these are not uniquely contributing to the fMRI signal. Moreover, HRV is an indirect proxy of ANS function via the resultant of ANS activity on the effectors, which are the receptors of sinus node cells<sup>53</sup>, and therefore HRV does not provide full characterization of ANS or

ANS-CNS interaction. Slightly different results were observed for the CSF/Vessels component when removing physiological noise. When BRV and HRV are regressed out, the component is still highly reproducible, whereas when RETROICOR predictors are regressed out, higher variability in the spatial distribution of the component is observed. This observation is not surprising when considering the association between the CSF/Vessels component with the vessel/perivascular pulsatility which is intrinsically dependent on the tonic circulation controlled by heart and respiration rhythm. When surrogate measures of heart activity and respiration are removed from the fMRI signals, the CSF/Vessels components are altered because they are highly related to blood/CSF flow.

As this is the first study performing nose fMRI, it is focused on to the demonstration of reproducibility of the method. Future studies are warranted to further explore the relation of nose fMRI activity with physiological and pathophysiological processes, including aging. Particularly, the relatively small number of participants spanning a broad age range challenges establishing inter-subject reproducibility at the group-level and obtaining robust statistical outcomes to quantify the nose network lateralization. Group comparisons were also generally limited by the lack of processing pipelines able to spatially normalize areas besides the brain across different individuals. Moreover, while no temporal or spatial smoothing was applied during data processing, spatial blurring still originated from the UTE radial acquisition, and from the substantial undersampling performed in order to maintain whole head coverage in a feasible acquisition time for fMRI analysis.

Moreover, the current experimental design did not include a specific olfactory stimulation task, thus future research needs to investigate if and how the nose signals are affected when the nose is engaged in olfactory activity. Finally, our experimental design lacked a systematic evaluation of the nasal cycle and of the nostril in use at the moment of each functional scans. Future studies need to include long-term monitoring of the nasal cycle (e.g. performing long-term rhinoflowmetry) as well as the acquisition of multiple anatomical images (e.g. before each functional scan) to detect possible changes in the open nostril during the MRI session.

Another limitation included the use of ultra-high field 7T magnet to conduct resting-state fMRI in humans. Future studies will need to establish feasibility of detecting nose signals at a lower magnetic field strength of 3T, more commonly available for human studies. Indeed, lower magnetic field strength is not expected to be detrimental for a flow-based functional contrast such as that of UTE fMRI, but at the same time image signal-to-noise is lower, which may still manifest in lower sensitivity to detect resting-state networks especially in single subjects. In fact, standard functional networks such as the DMN could be observed in group level analyses at 7T with UTE-fMRI (Fig. 2), however they were generally less reproducible across subjects than those detected with GE-EPI (data not shown). Also, whereas the origins of functional contrast with ultrashort/zero-TE is thought to be mostly blood flow and volume mediated, a detailed consideration on the multifactorial origin of the functional contrast, especially in the nose, is outside the scope of the current work and warrants future research.

The studies in awake mice conducted in this study were crucial to assess cross-species reproducibility, but they also presented several limitations. First, it was not possible to detect correlations with physiological signals because reliable physiological monitoring is not trivial with awake head-fixed unrestrained mice. Secondly, explaining the absence of unilaterality in the nose network in mice is hindered due to our lack of knowledge on the nasal cycle in this animal species. Finally, the absence of an observed CSF/Vessels network in mice was likely due to the fact that the spatial resolution of the functional zero-TE images was insufficient to highlight the small CSF spaces and arteries in mice, thus future studies will need to focus on acquiring higher spatial resolutions.

# Materials and methods Subjects

Seventeen healthy adult volunteers were recruited for the study, with the first 4 subjects scans dedicated to sequence testing and optimization. Thirteen subjects (age mean  $\pm$  SD = 44.6  $\pm$  17.6 years, 6 females/7 males) were included in analysis. Exclusion criteria included age below 18 years old, incompatibility with MR safety criteria, and major neurological and psychiatric pathologies. This study was carried out in accordance with the recommendations of The Code of Federal Regulations, Institutional Review Board. Written informed consent from all participants was obtained before the study in accordance with the Declaration of Helsinki. The protocol was approved by the Institutional Review Board: Human Subjects Committee of the University of Minnesota.

Five C57BL/6 mice (age mean  $\pm$  SD = 11.9  $\pm$  2.2 months, 1 female/4 males) were included in the preclinical application study. The animal studies were carried out in accordance with ARRIVE guidelines, and all animal procedures were approved by the Finnish Animal Experiment Board and conducted in accordance with the European Commission Directive 2010/63/EU guidelines.

# Data acquisition: human subjects

Head images were acquired on a 7T Siemens Magnetom scanner with a single transmit and 32-channel receive NOVA head coil. UTE fMRI acquisitions were performed using a slab selective UTE sequence with 1070 radial view to cover a FOV =  $192 \times 192 \times 192 \, \text{mm}^3$ , with a final spatial resolution of  $2 \times 2 \times 2 \, \text{mm}^3$ , time to acquire one radial view (repetition time, TR) = 1.4 ms, echo time (TE) = 0.12 ms, flip angle =  $2^{\circ}$ , time to acquire each 3D-volume (temporal resolution) = 1.5 s, 244 volumes collected. Three runs of UTE rsfMRI were performed for each subject with a mean time interval between run 1 and run 2 of 45 min  $\pm$  13 min, between run 1 and run 3 of 51 min  $\pm$  13 min and between run 2 and run 3 of 6 min  $\pm$  0.1 s. Gradient echo EPI (GE-EPI) fMRI acquisitions were performed using a 2D GE SMS/MB EPI with 95 slices, TR = 1.5 s TE = 22.2 ms, MB factor 4, FOV =  $256 \times 256$  and  $2 \times 2 \times 2 \, \text{mm}^3$  voxel size. In addition to the functional scans, two anatomical images were included in the protocol. An MP2RAGE<sup>54</sup> sequence was acquired with 240 slices, TR = 5000 ms, FOV =  $240 \times 225 \, \text{mm}^2$ ; flip angle =  $4^{\circ}$ , TE =  $2.27 \, \text{ms}$ , spatial resolution  $0.75 \times 0.75 \times 0.8 \, \text{mm}^3$ . A high-resolution UTE sequence was also acquired with the following parameters: 4096 radial view and 24 radial interleaves, FOV =  $192 \times 192 \times 192 \, \text{mm}^3$  with a final isotropic spatial resolution  $0.75 \, \text{mm}$ , TR = 3 ms, TE =  $0.11 \, \text{ms}$ , flip

angle = 3.5°. Throughout functional scanning, the physiological status of the subjects were monitored and recorded by means of a respiratory belt and a pulse plethysmograph using Siemens PMU systems (Erlangen, Germany) with both signals sampled at 400 Hz. The recording of the physiological signals was prolonged for 2 min after the end of each scan to obtain HRV and BRV measurement of the same size as the fMRI dataset (see section below *Data processing: physiological signals in humans*).

### Data acquisition: awake mice

Prior to awake imaging, mice underwent surgery where a headpost was placed on top of the skull. Briefly, mice were first anesthetized with isoflurane (5% induction and 2% maintenance in N2/O2 70%/30%). The skull was exposed and a custom-made headpost made of polytetrafluoroethylene or polychlorotrifluoroethylene was secured on the clean skull with dental cement. Carprofen (Rimadyl, Zoetis Finland Oy, 5 mg/kg by sub cutaneous injection) was given to treat post-surgical pain, and mice were allowed to recover at least three weeks. Subsequently, mice were habituated for awake imaging during a 14-day habituation protocol, which included gradual acclimation to the handling person, animal holder, head-fixation, ear plugs, and acoustic scanner noise. While being head-fixed in the imaging holder (up to 25 min), mice were standing on their feet on a slippery glass or acrylic glass surface without body restraint. Mice were positioned and removed from the imaging holder under moderate isoflurane anesthesia (1.5-2.0%). A positive reinforcement (sweetened hazelnut cocoa spread or 1% sucrose water) was given before and after each habituation or measurement session.

High-resolution anatomical images and resting-state fMRI data were acquired with MB-SWIFT sequences on a 9.4T (Varian, Palo Alto, CA, USA) system using a 22-mm transceiver surface RF-coil (Neos Biotec, Pamplona, Spain) covering nose and brain. For anatomical images, the acquisition parameters were the following: 4000 radial views, 16 stacks of spirals, four radiofrequency pulses per radial view, FOV =  $32 \times 32 \times 32 \times 32$  mm3, isotropic voxels of 0.125 mm3, TR=3 ms, flip angle=5.0°, excitation/acquisition bandwidths of 192/384 kHz, leading to total acquisition time of 4 min. To enhance contrast, a magnetization transfer pulse (sinc-shaped pulse,  $\gamma$ B1=125 Hz, offset=2000 Hz, pulse duration=20 ms) was given every 32 radial views. For fMRI, the acquisition parameters were the following: 2047 radial views, one spiral, two radiofrequency pulses per radial view, FOV=32×32×32 mm3, isotropic voxels of 0.5 mm3, TR=0.81 ms, flip angle=2.0°, excitation/acquisition bandwidths of 125/500 kHz, leading to time for single 3D-image of 1.7 s. Resting-state data were collected for 10–20 min (~350–700 volumes). Three out of 5 mice were scanned twice in two different days for a total of 8 datasets.

Mice were kept under isoflurane anesthesia during preparations and anatomical scans. Before fMRI, the administration of isoflurane was ceased, and the scan was started 2–3 min later when mice showed clear signs of being awake (e.g., whisker or limb movement). The behavior was monitored with an MRI-compatible video camera (12 M-i, MRC Systems GmbH, Heidelberg, Germany).

#### Data processing: physiological signals in humans

For processing and analysis of physiological signals, we used PhysioNet Cardiovascular Signal Toolbox implemented in MATLAB, python-based scripts to create fMRI predictors with physiological signals provided by BrainVoyager (https://support.brainvoyager.com/brainvoyager/available-tools/107-python-tools/413-physiological-noise-correction-in-python) and custom scripts. Pulse signals were imported in MATLAB, synchronized with the MRI acquisition, and then smoothed with a Savitzky-Golay FIR smoothing filter (order 3, frame size 67 samples). Pulse wave onsets were detected by analyzing the slope sum function, and time between successive wave onsets (PP intervals) were calculated. Abnormal values due to measurement instability were excluded by removing PP intervals lower than 0.33 s and higher than 1.5 s. Signals from the respiratory belt were also imported in MATLAB and synchronized with the MRI acquisition. Similarly to the pulse signal, respiration wave onsets were detected, and time between successive maximum peaks (RR intervals) were calculated. The PP and RR intervals were used to obtain heart rate variability (HRV) and breathing rate variability (BRV) time series. Particularly, the root-mean-square of successive differences in PP or RR intervals (RMSSD) was calculated in adjacent time windows of 100 s with a timestep of 1 s<sup>56</sup>. From the pulse and respiration signals, also the heart rate (HR) and the breathing rate (BR) were calculated as time difference between successive maximum peaks expressed in beat-per-minute (bpm) and respirations-per-minute (rpm) respectively.

Pulse and respiration signals were also used to calculate a basis set of sine and cosine Fourier series components extending to the 2rd harmonic (i.e. 4 terms) used to model the fluctuations arising from the cardiac and respiratory phase respectively according to the RETROICOR model<sup>25</sup>. Those 8 total predictors were used to model and remove the effect of physiological noise in the resting-state fMRI time series. Finally, all the obtained measures were resampled at the fMRI temporal resolution (1.5 s).

#### Data processing: resting-state fMRI in humans

Human fMRI data were processed using BrainVoyager QX (Brain Innovation, Maastricht, the Netherlands, www.brainvoyager.com) and custom MATLAB scripts. For the UTE data, the preprocessing steps included the removal of 4 dummy volumes and 3D rigid body motion correction using sinc interpolation and aligning all volumes to the first volume. No spatial nor temporal smoothing was applied. For GE-EPI data, the slice scan timing correction was performed in addition to the preprocessing steps of UTE.

After importing MP2RAGE anatomical series in BrainVoyager, background denoising was performed<sup>57</sup>. Functional data were aligned to anatomical data with manual adjustments and quality control, critically relevant in the case of UTE. High resolution anatomical UTE images were also co-registered to the respective MP2RAGE images using FSL FLIRT<sup>58</sup> and manual adjustments where needed and then imported in BrainVoyager. For group analysis, anatomical images were transformed to standard Montreal Neurological Institute (MNI) space via a template match normalization, and the same obtained transformation was used to normalize the

functional series. In the normalized space, group-level ICA were carried out on the preprocessed functional time series using the fast ICA algorithm<sup>59</sup> and the self-organizing group ICA algorithm<sup>60</sup>. The group-level ICA was performed with 30 independent components using two different masks: a brain-only mask obtained from the brain segmentation of the MNI template, and a brain-nose mask which included the brain-only mask and a manually drown mask covering the nose and the lower part of head within the field of view. An average (across subjects) anatomical image in MNI was also calculated and used to display group-level results.

Single subject ICA was also performed on the UTE rsfMRI data in the native subject's space in order to avoid unwanted effects of non-optimized alignments between subjects, specifically for areas outside the brain. Single subjects ICA was performed twice, estimating 30 and 20 independent components for each subject and applying a subject-specific manually drown mask including the brain and the nose. In order also to account for physiological noise, single-subject analysis was repeated in three additional different scenarios, namely by regressing out either the RETROICOR physiological predictors, or the BRV and HRV signals, or the mean time-courses in white matter and CSF. After each of these preprocessing steps, the ICA analysis was performed again with 30 ICs. Then, to facilitate the selection of similar ICs (compared to the original selected ones), the dice similarity coefficient was calculated between each ICs after corrections and the original ones. Components with the higher dice coefficients were visually inspected before being selected as ICs of interest.

#### Data processing: resting-state fMRI in awake mice

The MB-SWIFT data was reconstructed using RF-pulse deconvolution, gridding and iterative FISTA algorithm<sup>61</sup> volume-by-volume with 13 iterations. All MRI data was processed and analyzed using in-house Snakemake (https://snakemake.github.io/<sup>62</sup>), and Python (version 3.10, https://www.python.org/downloads/) scripts.

The reconstructed anatomical MB-SWIFT images were co-registered to a study-specific template using rigid and non-linear SyN registration<sup>63</sup> from Advanced Normalization Tools (ANTs; http://stnava.github.io/ANTs/<sup>64</sup>), . Functional data was manually motion-scrubbed to remove the influence of excessive motion on analyses, and the removed volumes were mean-interpolated using neighboring volumes. Motion-scrubbed functional data was co-registered to the functional template by using transformations from the anatomical co-registration. Data were spatially smoothed with a gaussian kernel of standard deviation of 0.4 mm with FSL toolbox (https://fsl.fmrib.ox.ac.uk/fsl/fslwiki).

Single subject ICA was performed using FSL MELODIC (https://fsl.fmrib.ox.ac.uk/fsl/fslwiki/MELODIC) toolbox estimating 30 components for each subject by using a manually drawn mask covering brain and nose. Similarly, 30 components were estimated group-wise.

# Statistical analysis

IC spatial maps at single-subject and group level were scaled to spatial z-score. Pearson's coefficient of correlation was calculated between the time-courses of the ICs of interest and each of the physiological signals time series (HRV, BRV, HR, BR) for each subject (when available). For group-level analysis, a linear mixed model was performed in MATLAB with resting-state fMRI component time-courses (each component of interest separately) as dependent variable and the four physiological measures as independent variables while the subjects and run variables were accounted as random effect variables. Results were considered significant after Bonferroni correction for multiple comparisons on the number of independent tests (n=2).

After hard thresholding of IC maps (for both humans and mice) removing values |z-score| < 2, and binarization, the dice similarity coefficient was calculated to assess the intra-subject reproducibility of estimated components across different runs and across different physiological noise corrections (for humans) and to assess the inter-subject reproducibility of estimated components (for mice).

#### Data availability

All data needed to evaluate the conclusions in the paper are present in the paper and/or the Supplementary Materials. The raw data and code used in the analysis are available upon request to of the corresponding author after satisfying regulatory requirements of material transfer agreements of the University of Minnesota.

Received: 21 August 2024; Accepted: 23 October 2024

# Published online: 01 November 2024

#### References

- 1. Khonsary, S. A. in Surg. Neurol. Int. 7 (2016). (Copyright: © 2016 Surgical Neurology International.
- Lochhead, J. J. & Thorne, R. G. Intranasal delivery of biologics to the central nervous system. Adv. Drug Deliv Rev. 64, 614–628. https://doi.org/10.1016/j.addr.2011.11.002 (2012).
- 3. Sarin, S., Undem, B., Sanico, A. & Togias, A. The role of the nervous system in rhinitis. *J. Allergy Clin. Immunol.* 118, 999–1016. https://doi.org/10.1016/j.jaci.2006.09.013 (2006).
- 4. Smith, D. H., Brook, C. D., Virani, S. & Platt, M. P. The inferior turbinate: An autonomic organ. *Am. J. Otolaryngol.* 39, 771–775. https://doi.org/10.1016/j.amjoto.2018.08.009 (2018).
- Wang, X. Y., Han, Y. Y., Li, G. & Zhang, B. Association between autonomic dysfunction and olfactory dysfunction in Parkinson's disease in southern Chinese. BMC Neurol. 19, 17. https://doi.org/10.1186/s12883-019-1243-4 (2019).
- 6. Lee, P. H., Yeo, S. H., Kim, H. J. & Youm, H. Y. Correlation between cardiac 123I-MIBG and odor identification in patients with Parkinson's disease and multiple system atrophy. *Mov. Disord.* 21, 1975–1977. https://doi.org/10.1002/mds.21083 (2006).
- Goldstein, D. S. & Sewell, L. Olfactory dysfunction in pure autonomic failure: Implications for the pathogenesis of Lewy body diseases. *Parkinsonism Relat. Disord.* 15, 516–520. https://doi.org/10.1016/j.parkreldis.2008.12.009 (2009).
- 8. Son, G. et al. Olfactory neuropathology in Alzheimer's disease: a sign of ongoing neurodegeneration. BMB Rep. 54, 295–304. https://doi.org/10.5483/BMBRep.2021.54.6.055 (2021).
- Schubert, C. R. et al. Olfaction and the 5-year incidence of cognitive impairment in an epidemiological study of older adults. J. Am. Geriatr. Soc. 56, 1517–1521. https://doi.org/10.1111/j.1532-5415.2008.01826.x (2008).

- 10. Doty, R. L. The olfactory vector hypothesis of neurodegenerative disease: is it viable? *Ann. Neurol.* **63**, 7–15. https://doi.org/10.100 2/ana.21327 (2008).
- Ogawa, S. et al. Intrinsic signal changes accompanying sensory stimulation: functional brain mapping with magnetic resonance imaging. Proc. Natl. Acad. Sci. U S A. 89, 5951–5955. https://doi.org/10.1073/pnas.89.13.5951 (1992).
- 12. Farzaneh, F., Riederer, S. J. & Pelc, N. J. Analysis of T2 limitations and off-resonance effects on spatial resolution and artifacts in echo-planar imaging. *Magn. Reson. Med.* 14, 123–139. https://doi.org/10.1002/mrm.1910140112 (1990).
- 13. Jezzard, P. & Balaban, R. S. Correction for geometric distortion in echo planar images from B0 field variations. *Magn. Reson. Med.* 34, 65–73. https://doi.org/10.1002/mrm.1910340111 (1995).
- 14. Andersson, J. L., Skare, S. & Ashburner, J. How to correct susceptibility distortions in spin-echo echo-planar images: application to diffusion tensor imaging. *Neuroimage*. 20, 870–888. https://doi.org/10.1016/S1053-8119(03)00336-7 (2003).
- Bracher, A. K. et al. Feasibility of ultra-short echo time (UTE) magnetic resonance imaging for identification of carious lesions. Magn. Reson. Med. 66, 538–545. https://doi.org/10.1002/mrm.22828 (2011).
- 16. Gatehouse, P. D. & Bydder, G. M. Magnetic resonance imaging of short T2 components in tissue. Clin. Radiol. 58, 1–19. https://doi.org/10.1053/crad.2003.1157 (2003).
- Bergin, C. J., Pauly, J. M. & Macovski, A. Lung parenchyma: projection reconstruction MR imaging. *Radiology*. 179, 777–781. https://doi.org/10.1148/radiology.179.3.2027991 (1991).
- 18. Weiger, M., Pruessmann, K. P. & Hennel, F. MRI with zero echo time: hard versus sweep pulse excitation. *Magn. Reson. Med.* **66**, 379–389. https://doi.org/10.1002/mrm.22799 (2011).
- 19. Idiyatullin, D., Corum, C., Park, J. Y. & Garwood, M. Fast and quiet MRI using a swept radiofrequency. *J. Magn. Reson.* **181**, 342–349. https://doi.org/10.1016/j.jmr.2006.05.014 (2006).
- 20. Idiyatullin, D., Corum, C. A., Garwood, M. & Multi-Band, S. W. I. F. T. J. Magn. Reson. 251, 19–25 https://doi.org/10.1016/j.jmr.2014.11.014 (2015).
- Lehto, L. J. et al. MB-SWIFT functional MRI during deep brain stimulation in rats. Neuroimage. 159, 443

  –448. https://doi.org/10.1016/j.neuroimage.2017.08.012 (2017).
- Paasonen, J. et al. Whole-brain studies of spontaneous behavior in head-fixed rats enabled by zero echo time MB-SWIFT fMRI. Neuroimage. 250, 118924. https://doi.org/10.1016/j.neuroimage.2022.118924 (2022).
- Kim, M. J., Jahng, G. H., Lee, S. Y. & Ryu, C. W. Functional magnetic resonance imaging with an ultrashort echo time. Med. Phys. 40, 022301. https://doi.org/10.1118/1.4773035 (2013).
- 24. Mangia, S. et al. S. in International Society of Magnetic Resonance in Medicine.
- 25. Glover, G. H., Li, T. Q. & Ress, D. Image-based method for retrospective correction of physiological motion effects in fMRI: RETROICOR. *Magn. Reson. Med.* 44, 162–167. https://doi.org/10.1002/1522-2594(200007)44:1<162::aid-mrm23>3.0.co;2-e (2000)
- Werntz, D. A. & Bickford, R. G. Shannahoff-Khalsa, D. Selective hemispheric stimulation by unilateral forced nostril breathing. Hum. Neurobiol. 6, 165–171 (1987).
- Price, A. & Eccles, R. Nasal airflow and brain activity: is there a link? J. Laryngol Otol. 130, 794–799. https://doi.org/10.1017/S002 2215116008537 (2016).
- Shannahoff-Khalsa, D. S., Boyle, M. R. & Buebel, M. E. The effects of unilateral forced nostril breathing on cognition. Int. J. Neurosci. 57, 239–249. https://doi.org/10.3109/00207459109150697 (1991).
- 29. Gureviciene, I. et al. Orientation selective stimulation with tetrahedral electrodes of the rat infralimbic cortex to indirectly target the amygdala. *Front. Neurosci.* 17, 1147547. https://doi.org/10.3389/fnins.2023.1147547 (2023).
- Laakso, H. et al. Spinal cord fMRI with MB-SWIFT for assessing epidural spinal cord stimulation in rats. Magn. Reson. Med. 86, 2137–2145. https://doi.org/10.1002/mrm.28844 (2021).
- Lehto, L. J. et al. Orientation selective deep brain stimulation of the subthalamic nucleus in rats. *Neuroimage*. 213, 116750. https://doi.org/10.1016/j.neuroimage.2020.116750 (2020).
- 32. Lehto, L. J. et al. Tuning Neuromodulation Effects by Orientation Selective Deep Brain Stimulation in the Rat Medial Frontal Cortex. Front. Neurosci. 12, 899. https://doi.org/10.3389/fnins.2018.00899 (2018).
- 33. Wu, L. et al. Orientation selective DBS of entorhinal cortex and medial septal nucleus modulates activity of rat brain areas involved in memory and cognition. Sci. Rep. 12, 8565. https://doi.org/10.1038/s41598-022-12383-2 (2022).
- Paasonen, J. et al. Multi-band SWIFT enables quiet and artefact-free EEG-fMRI and awake fMRI studies in rat. Neuroimage. 206, 116338. https://doi.org/10.1016/j.neuroimage.2019.116338 (2020).
- Raichle, M. E. The brain's default mode network. Annu. Rev. Neurosci. 38, 433–447. https://doi.org/10.1146/annurev-neuro-07101 3-014030 (2015).
- 36. Shaffer, F. & Ginsberg, J. P. An Overview of Heart Rate Variability Metrics and Norms. Front. Public. Health. 5, 258. https://doi.org/10.3389/fpubh.2017.00258 (2017).
- 37. Low, P. A. Autonomic nervous system function. J. Clin. Neurophysiol. 10, 14–27. https://doi.org/10.1097/00004691-199301000-00 003 (1993).
- 38. Williams, M. R. & Eccles, R. The nasal cycle and age. *Acta Otolaryngol.* 135, 831–834. https://doi.org/10.3109/00016489.2015.102 8592 (2015).
- Stoksted, P. & Thomsen, K. A. Changes in the nasal cycle under stellate ganglion block. Acta Otolaryngol. Suppl. 109, 176–181. https://doi.org/10.3109/00016485309132517 (1953).
- Bamford, O. S. & Eccles, R. The central reciprocal control of nasal vasomotor oscillations. Pflugers Arch. 394, 139–143. https://doi.org/10.1007/BF00582915 (1982).
- 41. Bojsen-Moller, F. & Fahrenkrug, J. Nasal swell-bodies and cyclic changes in the air passage of the rat and rabbit nose. *J. Anat.* 110, 25–37 (1971).
- 42. Parthasarathy, K. & Bhalla, U. S. Laterality and symmetry in rat olfactory behavior and in physiology of olfactory input. *J. Neurosci.* 33, 5750–5760. https://doi.org/10.1523/JNEUROSCI.1781-12.2013 (2013).
- 43. Piechnik, S. K., Evans, J., Bary, L. H., Wise, R. G. & Jezzard, P. Functional changes in CSF volume estimated using measurement of water T2 relaxation. *Magn. Reson. Med.* 61, 579–586. https://doi.org/10.1002/mrm.21897 (2009).
- 44. Williams, S. D. et al. Neural activity induced by sensory stimulation can drive large-scale cerebrospinal fluid flow during wakefulness in humans. *PLoS Biol.* 21, e3002035. https://doi.org/10.1371/journal.pbio.3002035 (2023).
- 45. Fultz, N. E. et al. Coupled electrophysiological, hemodynamic, and cerebrospinal fluid oscillations in human sleep. *Science*. **366**, 628–631. https://doi.org/10.1126/science.aax5440 (2019).
- 46. Mestre, H. et al. Flow of cerebrospinal fluid is driven by arterial pulsations and is reduced in hypertension. *Nat. Commun.* 9, 4878. https://doi.org/10.1038/s41467-018-07318-3 (2018).
- 47. Mehta, N. H. et al. The Brain-Nose Interface: A Potential Cerebrospinal Fluid Clearance Site in Humans. Front. Physiol. 12, 769948. https://doi.org/10.3389/fphys.2021.769948 (2021).
- 48. de Leon, M. J. et al. Cerebrospinal Fluid Clearance in Alzheimer Disease Measured with Dynamic PET. J. Nucl. Med. 58, 1471–1476. https://doi.org/10.2967/jnumed.116.187211 (2017).
- 49. Sass, L. R. et al. Non-invasive MRI quantification of cerebrospinal fluid dynamics in amyotrophic lateral sclerosis patients. *Fluids Barriers CNS*. 17, 4. https://doi.org/10.1186/s12987-019-0164-3 (2020).
- 50. de Leon, M. J. et al. Longitudinal cerebrospinal fluid tau load increases in mild cognitive impairment. *Neurosci. Lett.* 333, 183–186. https://doi.org/10.1016/s0304-3940(02)01038-8 (2002).

- 51. Benveniste, H. et al. Glymphatic Cerebrospinal Fluid and Solute Transport Quantified by MRI and PET Imaging. *Neuroscience*. 474, 63–79. https://doi.org/10.1016/j.neuroscience.2020.11.014 (2021).
- 52. Li, J. et al. Whole-brain mapping of mouse CSF flow via HEAP-METRIC phase-contrast MRI. Magn. Reson. Med. 87, 2851–2861. https://doi.org/10.1002/mrm.29179 (2022).
- 53. Zygmunt, A. & Stanczyk, J. Methods of evaluation of autonomic nervous system function. *Arch. Med. Sci.* 6, 11–18. https://doi.org/10.5114/aoms.2010.13500 (2010).
- Marques, J. P. et al. MP2RAGE, a self bias-field corrected sequence for improved segmentation and T1-mapping at high field. Neuroimage. 49, 1271–1281. https://doi.org/10.1016/j.neuroimage.2009.10.002 (2010).
- 55. Vest, A. N. et al. An open source benchmarked toolbox for cardiovascular waveform and interval analysis. *Physiol. Meas.* 39, 105004. https://doi.org/10.1088/1361-6579/aae021 (2018).
- Kassinopoulos, M., Harper, R. M., Guye, M., Lemieux, L. & Diehl, B. Altered Relationship Between Heart Rate Variability and fMRI-Based Functional Connectivity in People With Epilepsy. Front. Neurol. 12, 671890. https://doi.org/10.3389/fneur.2021.671890 (2021).
- 57. O'Brien, K. R. et al. Robust T1-weighted structural brain imaging and morphometry at 7T using MP2RAGE. *PLoS One.* **9**, e99676. https://doi.org/10.1371/journal.pone.0099676 (2014).
- 58. Jenkinson, M., Bannister, P., Brady, M. & Smith, S. Improved optimization for the robust and accurate linear registration and motion correction of brain images. *Neuroimage*. 17, 825–841. https://doi.org/10.1016/s1053-8119(02)91132-8 (2002).
- Hyvarinen, A. Blind source separation by nonstationarity of variance: a cumulant-based approach. *IEEE Trans. Neural Netw.* 12, 1471–1474. https://doi.org/10.1109/72.963782 (2001).
- Esposito, F. et al. Independent component analysis of fMRI group studies by self-organizing clustering. Neuroimage. 25, 193–205. https://doi.org/10.1016/j.neuroimage.2004.10.042 (2005).
- 61. Beck, A., Teboulle, M. A. Fast Iterative Shrinkage-Thresholding Algorithm for Linear Inverse Problems. SIAM J. Imaging Sci. 2, 183–202. https://doi.org/10.1137/080716542 (2009).
- Koster, J. & Rahmann, S. Snakemake–a scalable bioinformatics workflow engine. Bioinformatics. 28, 2520–2522. https://doi.org/1 0.1093/bioinformatics/bts480 (2012).
- 63. Avants, B. B., Epstein, C. L., Grossman, M. & Gee, J. C. Symmetric diffeomorphic image registration with cross-correlation: evaluating automated labeling of elderly and neurodegenerative brain. *Med. Image Anal.* 12, 26–41. https://doi.org/10.1016/j.med ia.2007.06.004 (2008).
- 64. Avants, B. B., Tustison, N. & Song, G. Advanced Normalization Tools: V1.0. Insight J. 2, 1–35. https://doi.org/10.54294/uvnhin (2009).

## **Acknowledgements**

We thank Dr. Naoharu Kobayashi and Dr. Edward Auerbach for technical support, and the volunteers for their participation in the study.

# **Author contributions**

Conceptualization: PF, DLR, HT, SMi, SMa; Data curation: SP, JP, SMi; Formal Analysis: SP, RAS, JP; Investigation: SP, JP, PS; Methodology: MG, OG, SMi, SMa; Project administration: GJM, OG, SMi, SMa; Software: SP, RAS; Supervision: DLG, LEE, OG, SMi, SMa; Visualization: SP, JP, SMa; Writing – original draft: SP, SMi, SMa; Writing – review & editing: SP, JP, PS, RAS, HT, PF, DLR, LEE, MG, GJM, OG, SMi, SMa.

#### Funding

National Institutes of Health grant P41 EB027061. The content is solely the responsibility of the authors and does not necessarily represent the official views of the funding agencies.

# **Declarations**

#### Competing interests

The authors declare no competing interests.

# Additional information

**Supplementary Information** The online version contains supplementary material available at https://doi.org/10.1038/s41598-024-77615-z.

Correspondence and requests for materials should be addressed to S.M.

**Reprints and permissions information** is available at www.nature.com/reprints.

**Publisher's note** Springer Nature remains neutral with regard to jurisdictional claims in published maps and institutional affiliations.

**Open Access** This article is licensed under a Creative Commons Attribution-NonCommercial-NoDerivatives 4.0 International License, which permits any non-commercial use, sharing, distribution and reproduction in any medium or format, as long as you give appropriate credit to the original author(s) and the source, provide a link to the Creative Commons licence, and indicate if you modified the licensed material. You do not have permission under this licence to share adapted material derived from this article or parts of it. The images or other third party material in this article are included in the article's Creative Commons licence, unless indicated otherwise in a credit line to the material. If material is not included in the article's Creative Commons licence and your intended use is not permitted by statutory regulation or exceeds the permitted use, you will need to obtain permission directly from the copyright holder. To view a copy of this licence, visit <a href="http://creativecommons.org/licenses/by-nc-nd/4.0/">http://creativecommons.org/licenses/by-nc-nd/4.0/</a>.

© The Author(s) 2024